Electronic Supplementary Information (ESI)

Au_3-decorated graphene as a sensing platform for O_2 adsorption and desorption kinetics

Guillaume Libeert[1], Ramasamy Murugesan[2], Márton Guba[3], Wout Keijers[1], Simon Collienne[4], Bart Raes[1], Steven Brems[5], Stefan De Gendt[5,6], Alejandro Silhanek[4], Tibor Höltzl[3,7], Michel Houssa[2,5], Joris Van de Vondel[1], Ewald Janssens[1]

[1]*Quantum Solid-State Physics, Department of Physics and Astronomy, KU Leuven, Leuven, Belgium*

[2]*Semiconductor Physics Laboratory, Department of Physics and Astronomy, KU Leuven, Leuven, Belgium*

[3]*Budapest University of Technology and Economics, Department of Inorganic and Analytical Chemistry and MTA-BME Computation driven research group, Budapest, Hungary*

[4]*Experimental Physics of Nanostructured Materials, Q-MAT, CESAM, Université de Liege, Sart Tilman, Belgium*

[5]*Imec, Leuven, Belgium*

[6]*Division of Molecular Design and Synthesis, Department of Chemistry, KU Leuven, Leuven, Belgium*

[7] *Furukawa Electric Institute of Technology Ltd., Budapest, Hungary*

Content

1. Device fabrication

Graphene on Si++/SiO_2 (300 nm) substrates are grown using platinum-based chemical vapor deposition (Pt-CVD).[1] An etch mask is fabricated by spin-coating the sample with PMMA (Poly(methyl methacrylate), ALLRESIST AR 679.035) at 7 kRPM and by patterning with a customized Raith Electron Beam Lithography (EBL) platform. The exposed resist is removed with a developer consisting of a 1:1 mixture of methyl isobutyl ketone (MIBK) and isopropyl alcohol (IPA). The redundant graphene is removed by Reactive Ion Etching (RIE), followed by a lift-off process using acetone and subsequent IPA rinsing. A second mask for Ti/Au contacts is fabricated by spin-coating a layer of PMMA at 7 kRPM and a layer of PMMA-MA (PMMA-copolymer, ALLRESIST AR 617.04)) at 4 kRPM and by EBL patterning and developing with MIBK:IPA. Next, a 4 nm Ti layer and a 20 nm Au layer were deposited by molecular beam epitaxy (MBE) with a typical growth rate of 0.2 Å/s, followed by a lift-off process using acetone and subsequent IPA rinsing.

2. Calculation of collision frequency

The collision frequency Z of the O_2 molecules with the deposited Au_3 clusters equals the number of colliding molecules $N_{\mathrm{O_2,coll}}$ per time Δt. $N_{\mathrm{O_2,coll}}$ can be calculated by dividing the total impulse J exerted on all colliding oxygen molecules during Δt by the average change in momentum of an O_2 molecule Δp and by multiplying with the cluster coverage C:

$$Z = \frac{N_{\mathrm{O_2,coll}}}{\Delta t} = \frac{C}{\Delta t}\frac{J}{\Delta p} = \frac{3 \cdot n_{\mathrm{Au_3}}}{n_{\mathrm{monolayer}}}\frac{PA}{2}\sqrt{\frac{\pi}{mk_BT}} = \frac{3 \cdot N_{\mathrm{Au_3}}}{n_{\mathrm{monolayer}}}\frac{P}{2}\sqrt{\frac{\pi}{mk_BT}}$$

With P the pressure in the chamber (10^{-4} mbar), A the area of the investigated graphene strip (210 µm^2), m the mass of an O_2 molecule (32 amu), k_B the Boltzmann constant ($8.617 \cdot 10^{-5}$ eV K^{-1}) and T the temperature of the O_2 gas during exposure (293 K). The density of deposited clusters $n_{\mathrm{Au_3}}$ is 10^{14} clusters/cm^2. Since each cluster contains 3 atoms, $3 \cdot 10^{14}$ atoms/cm^2 and the density of a hexagonal-close packed Au monolayer $n_{\mathrm{monolayer}}$ is $1.52 \cdot 10^{15}$ atoms/cm^2 [2]. In the last step $n_{\mathrm{Au_3}} = N_{\mathrm{Au_3}}/A$ was used.

3. Computed geometries and band structure

The most stable configuration for a Au_3 cluster on the graphene layer corresponds to a bridge position, with an Au-C bond length of 2.3 Å. The obtained results are also in excellent agreement with those of Srivastava et al.[3]

Fig. S1 presents the energetically favorable structures of the graphene supported Au_3 cluster without (top) and with (bottom) adsorbed oxygen molecule. The optimized geometry of the metal cluster does not change significantly in the absence of the oxygen molecule.

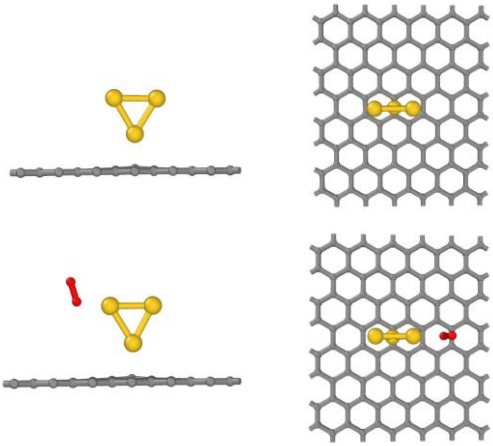

Fig. S1: Optimized geometries of Au3/graphene (top) and O2/Au3/graphene (bottom). A side view (left) and top view (right) are given.

From the computed band structure shown in Fig. S2 (right), it is found that the Au_3 cluster n-dopes graphene, as can be clearly seen from the downward shifting of the Dirac point relative to the Fermi level. Since we used a 6x6 supercell in the calculations, the Dirac points are folded into the gamma point. That is the reason the Dirac cone appears in the gamma point of the computed band structure. The calculated doping density for this system is 0.1154 x 10^{13} cm^{-2} charge carriers or 0.0217 e/cluster.

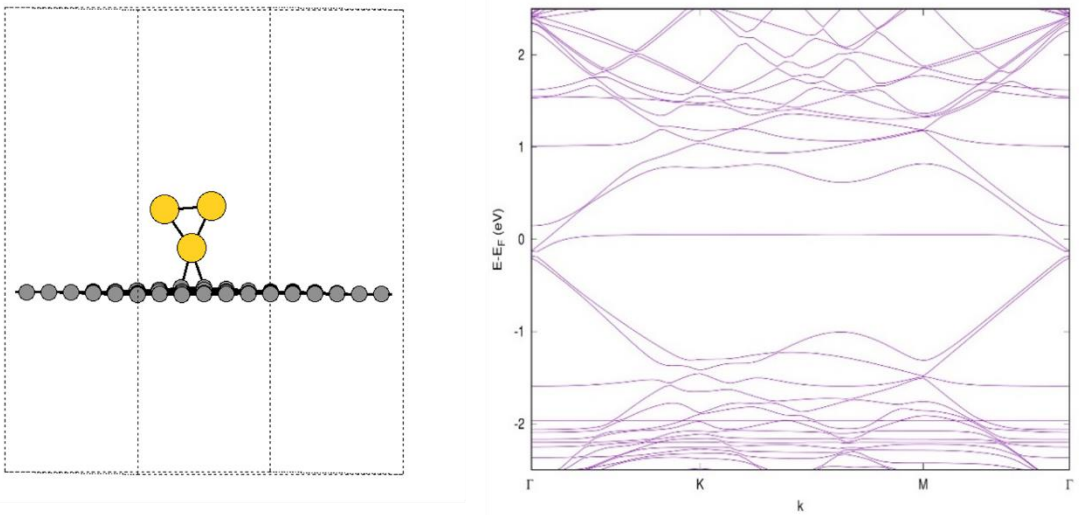

Fig. S2: The relaxed geometry with Au_3 cluster in a bridge position on graphene (left) and its computed band structure (right).

Similar geometrical relaxations were performed for the O_2 adsorbed and desorbed state of the Au_3/graphene system, as shown in Fig. S3 (left). The O_2 molecule bond length is elongated upon adsorption to the Au_3 cluster, from 1.23 Å in gas phase to 1.30 Å on Au_3/graphene. This indicates that

electrons are transferred to the oxygen molecule when O_2 is adsorbed on Au_3/graphene. This charge transfer is confirmed by the band structure show in Fig. S3 (right), in which the Dirac point is shifted above the Fermi level, indicating the hole-doping of graphene by Au_3/O_2. The doping density estimated from the band structure is 0.1137 x10^{13} cm^{-2} i.e., 0.0214 hole/O_2-cluster.

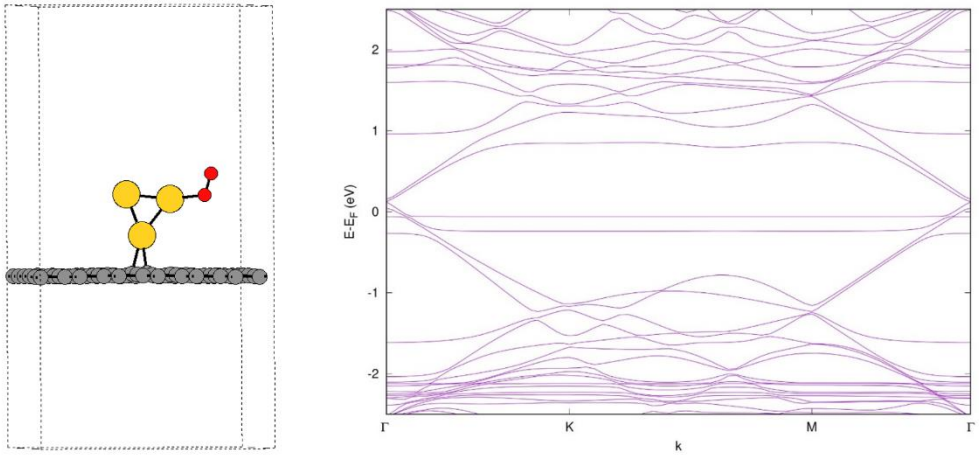

Fig. S3: The relaxed geometry obtained for an adsorbed oxygen molecule on Au_3/graphene (left) and its computed band structure (right).

4. Relation between resistivity measurements and shift in V_{CNP}

During the annealing cycles, the back-gate voltage is chosen such that the derivative of the sheet resistivity with respect to the back-gate voltage is maximal. Between the current pulses, the graphene sheet resistivity is measured. These values can be converted to shifts in V_{CNP}. To prove this, we must first approximate the curve of the sheet resistivity as a function of back-gate voltage at its point of highest derivative by a linear curve. This is illustrated in Fig. S4 and the mathematical justification is given below. The sheet resistivity as a function of back-gate/induced number of charge carriers is given by[4]:

$$\rho = \frac{1}{\sqrt{\sigma_{min}^2 + (ne\mu)^2}} + R_{SR}$$

With $n = \alpha(V_g - V_{\mathrm{CNP}})$ the charge carrier density per cm^2, α a constant that depends on the thickness of the silica layer and which in our case equals $7.2 \cdot 10^{10}$ V^{-1} cm^{-2}, e the electron charge in Coulomb, μ the electron mobility in cm^2/Vs, σ_{min} the minimal sheet conductivity in Siemens and R_{SR} the short range resistivity in Ohm. The derivative with respect to n is given by:

$$\frac{d\rho}{dn} = -n(e\mu)^2\left(\sigma_{min}^2 + (ne\mu)^2\right)^{-\frac{3}{2}}.$$

The derivative is maximal at the point where the second derivative is zero. The second derivative with respect to *n* is given by:

$$\frac{d^2\rho}{dn^2} = 3n^2(e\mu)^4\left(\sigma_{min}^2 + (ne\mu)^2\right)^{-5/2} - (e\mu)^2\left(\sigma_{min}^2 + (ne\mu)^2\right)^{-3/2}.$$

The second derivative is zero if

$$\frac{d^2\rho}{dn^2} = 0 \iff 2(ne\mu)^2 - \sigma_{min}^2 = 0$$

$$\iff n = \pm\frac{\sigma_{min}}{\sqrt{2}e\mu}.$$

This solution corresponds to $n \approx \pm 3 \cdot 10^{11}$ charge carriers/cm^2 for typical values. These are the inflection points of the sheet resistivity curve.

Since the number of induced charge carriers n is given by $\alpha\left(V_g - V_{\mathrm{CNP}}\right)$, the sheet resistivity can be written as:

$$\rho = \frac{1}{\sqrt{\sigma_{min}^2 + \left(\alpha e\mu\left(V_g - V_{\mathrm{CNP}}\right)\right)^2}} + R_{SR}$$

At the positive inflection point, $V_{g1} = \sigma_{min}/\sqrt{2}e\mu\alpha + V_{CNP}$, we can approximate the sheet resistivity by a Taylor expansion:

$$\rho(V_g) = \rho(V_{g1}) + \left.\frac{d\rho}{dV_g}\right|_{V_{g1}} (V_g - V_{g1})$$

$$= \sqrt{\frac{2}{3\sigma_{min}^2} + R_{SR} - \left(\sigma_{min}^2 + \left(\alpha e\mu\left(V_{g1} - V_{\mathrm{CNP}}\right)\right)^2\right)^{-3/2}\left(\alpha e\mu\left(V_{g1} - V_{CNP}\right)\right)(\alpha e\mu)\left(V_g - V_{g1}\right)}$$

$$= -\frac{2}{3\sqrt{3}}\frac{\alpha e\mu}{\sigma_{min}^2}\left(V_g - V_{\mathrm{CNP}}\right) + \frac{8}{3\sqrt{6}}\frac{1}{\sigma_{min}} + R_{SR}$$

As can be seen from this expression, ρ varies linearly with V_g around V_{g1}. From this formula, it follows that with the following data transformation, the shift in charge neutrality point can be obtained from resistivity measurements at back-gate value V_{g1}:

$$\frac{\rho_s - \rho_{s,i}}{\rho_{s,f} - \rho_{s,i}} = \frac{-\left(2\alpha e\mu\rho_{max}^2/3\sqrt{3}\right)\left(V_{g1} - V_{\mathrm{CNP}}\right) + \left(2\alpha e\mu\rho_{max}^2/3\sqrt{3}\right)\left(V_{g1} - V_{\mathrm{CNP}i}\right)}{-\left(2\,\alpha e\mu\rho_{max}^2/3\sqrt{3}\right)\left(V_{g1} - V_{\mathrm{CNP}f}\right) + \left(2\alpha e\mu\rho_{max}^2/3\sqrt{3}\right)\left(V_{g1} - V_{\mathrm{CNP}i}\right)}$$

$$= \frac{V_{\mathrm{CNP}i} - V_{\mathrm{CNP}}}{V_{\mathrm{CNP}i} - V_{\mathrm{CNP}f}}$$

$$\Rightarrow \frac{\rho_s - \rho_{s,i}}{\rho_{s,f} - \rho_{s,i}}\left(V_{\mathrm{CNP}i} - V_{\mathrm{CNP}f}\right) = V_{\mathrm{CNP}i} - V_{\mathrm{CNP}} = -\Delta V_{\mathrm{CNP}}$$

where $\rho_{s,i}$ and $\rho_{s,f}$ are the sheet resistivity values and $V_{\mathrm{CNP}i}$ and $V_{\mathrm{CNP}f}$ are the charge neutrality points, before and after the annealing procedure respectively.

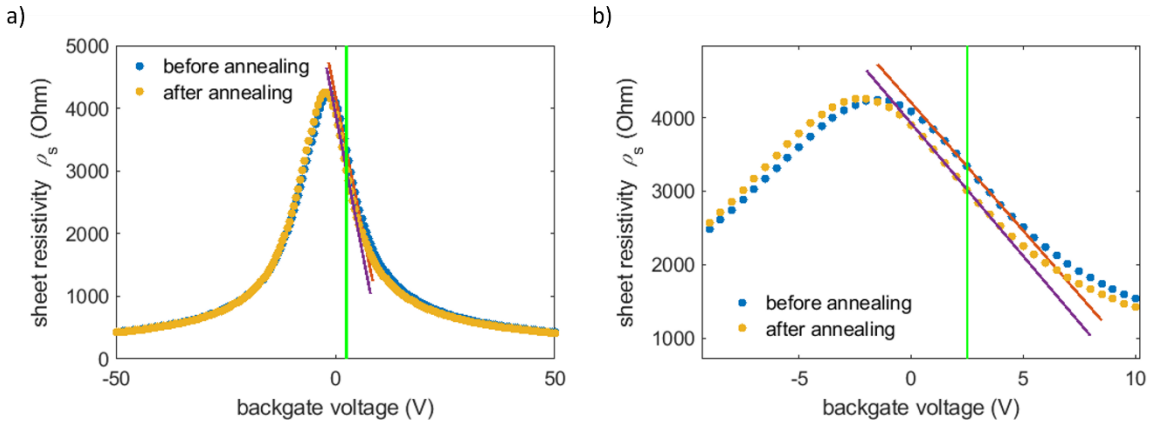

Fig. S4: a) Effect of annealing after oxygen exposure on the field-effect characteristic $\rho_s(V_g)$: the blue curve is before and the yellow curve after an annealing routine. b) zoom of panel a) around the point of highest derivative (in this case 2.5 V, indicated by the green line), the $\rho_s(V_g)$ has been approximated by a linear fit.

5. Power dissipation and temperature profile simulations

To model the power dissipation and the temperature profile along the graphene strip when a current is applied, a formalism based on the method developed by Bae et al in ref. 5 was used. In ref. 5, the temperature profile of a graphene strip under voltage bias inferred from infrared microscopy was found to be in good agreement with a finite-element simulation.

In our work, the graphene was heated by applying large source-drain biases and consequently large currents. Fig. S5 presents a schematic overview of the device. The Si++/SiO_2/G represents a parallel plate capacitor, so the voltage difference over the SiO_2 layer, $V_{\mathrm{SiO_2}}$, determines the induced carrier density in the graphene strip. For a small current, like the 1 µA used for the electrical characterization of the device, the source-drain voltage bias is negligible compared to the gate voltage V_g, and $V_{\mathrm{SiO_2}}$ will be, to a very good approximation, equal to V_g over the entire surface of the graphene strip. However, for bias currents in the order of mA, like the currents used to anneal the graphene strip, this hypothesis no longer holds. In that case the source-drain voltage V_{SD} will be in the order of tens of volts, and $V_{\mathrm{SiO_2}}$ is equal to $V_g - V_x$, where V_x is the position-dependent potential in the graphene strip (note that the voltage detector indicated by ΔV_x in Fig. S5 measures the difference in V_x between the two voltage contacts of the device). As a result, $V_{\mathrm{SiO_2}}$, and consequently also the induced number of charge carriers and the local sheet resistivity of the graphene device, become a function of position.

The finite-element simulation divides the graphene strip into $z = 10^6$ rectangles, with length 45 µm/z (45 µm being the length of the graphene strip). The evolution of the potential in the graphene V_x is then calculated as follows. In a first step, for the rectangle n, $V_{\mathrm{SiO_2}}$ is calculated with the formula $V_g - V_{n,x}$, with $V_{n,x}$ the graphene potential in rectangle n.[1] In a second step, the sheet resistivity of the rectangle is calculated with the formula $\rho = \frac{1}{\sqrt{\sigma_{\min}^2 + \left(\alpha\left(V_{\mathrm{SiO_2}} - V_{\mathrm{CNP}}\right)e\mu\right)^2}} + R_{\mathrm{SR}}$, where $\sigma_{\min}$, R_{SR} and μ were determined by fitting the sheet resistivity curve measured for a bias current of 1 µA (so when $V_{\mathrm{SiO_2}} \approx V_g$). The resistance of the rectangle is obtained by the formula $R = \rho \cdot \left(\frac{L}{W}\right)$ (where the width W varies over the graphene strip). In a third step, the resulting voltage difference ΔV over the rectangle is calculated with Ohm's law: $\Delta V = R \cdot I$, and the potential $V_{n+1,x}$ of rectangle $n+1$ is calculated as $V_{n+1,x} = V_{n,x} + \Delta V$. This procedure is applied sequentially for all rectangles in the graphene strip and in this way the evolution of V_x is obtained for the entire graphene strip. Since ΔV_x was measured experimentally during each annealing step, a comparison between experiment and simulation is possible, as shown in Fig. S6(a). In Fig. S6(b), the comparison between simulated and measured resistance is shown. As can be seen, the model reproduces both the orders of magnitude and the general trend of the experimental data, but not the exact data. This is mainly caused by the fact that the shift of the charge neutrality point during annealing was not taken into account. This shift in charge neutrality point during annealing cannot be measured experimentally, and is therefore left as a fitting parameter. In Fig. S7, the comparison between simulation and experiment is shown when V_{CNP} is left as a fitting parameter. In Fig. S8, the evolution of the fit parameter V_{CNP} is shown during annealing, as a function of the applied annealing current.

For each applied annealing current, the sheet resistivity profile $\rho(x)$ and the induced electron density $n(x) = \alpha(V_g - V_x - V_{CNP})$ is obtained over the entire graphene strip. The results are shown in Fig. S9 for applied annealing currents of 0.1 and 2.3 mA. Note that the sheet resistivity is maximal when the

(1) The calculation starts with the one closest to the drain, where V_x is zero (the drain is connected to the ground), so $V_{\mathrm{SiO_2}} = V_g$ for this rectangle. This gives an initial value for $V_{\mathrm{SiO_2}}$.

induced electron density is minimal. In Fig. S9(b), the induced electron density becomes negative for a part of the graphene strip, indicating that in this region, holes become the majority charge carriers.

Because the evolution of the sheet resistivity ρ and the graphene voltage V_x are simulated over the entire graphene strip, the power dissipation profile and consequently the temperature profile can be calculated using the heat transfer equation:[5]

$$Ak\frac{d^2T}{dx^2} - I\frac{dV_x}{dx} - g(T - T_0) = 0$$

With $A = Wh$ the graphene cross section (with h the thickness of the graphene equal to 0.34 nm), k the thermal conductivity of graphene, equal to 600 W/mK, $g = 1/\left(L(R_{\mathrm{ox}} + R_{\mathrm{Si}})\right)$ a thermal conductance to the substrate per unit length, $R_{\mathrm{ox}} = t_{\mathrm{ox}}/WLk_{\mathrm{ox}}$ (with t_{ox} the thickness of the substrate equal to 300 nm and k_{ox} the thermal conductivity of SiO_2 equal to 1.4 W/mK), $R_{\mathrm{Si}} = 1/\left(2k_{\mathrm{Si}}\sqrt{WL}\right)$ (with k_{Si} the thermal conductivity of Si equal to 130 W/mK), L the length of the graphene rectangle and T_0 the ambient temperature (in this case 293K).[5]

The heat transfer equation can be discretized with the finite difference method as

$$Ak\frac{T(x+L) - 2T(x) + T(x-L)}{\Delta x^2} - I\frac{V_x(x+L) - V_x(x)}{\Delta x} - \frac{T(x) - T_0}{\Delta x(R_{\mathrm{ox}} + R_{\mathrm{Si}})} = 0$$

With the simulated V_x profile, a value can be obtained for $T(x+L)$ when the values for $T(x)$ and $T(x-L)$ are known. By applying this formula sequentially to all graphene rectangles, the temperature profile can be obtained. The results are shown for different annealing currents in Fig. S10. Note that the temperature profiles were smoothed with a moving average filter because the finite difference method used to solve the heat transfer equation introduces fluctuations on the final result. As can be seen in Fig. S10, the temperature profiles are not uniform across the graphene strip, which is a direct consequence of the non-uniform sheet resistivity profiles shown in Fig. S9. In Fig. S10, the position of the voltage contacts of the graphene are indicated. The temperature in the probed part of the graphene is maximal at the voltage contact.

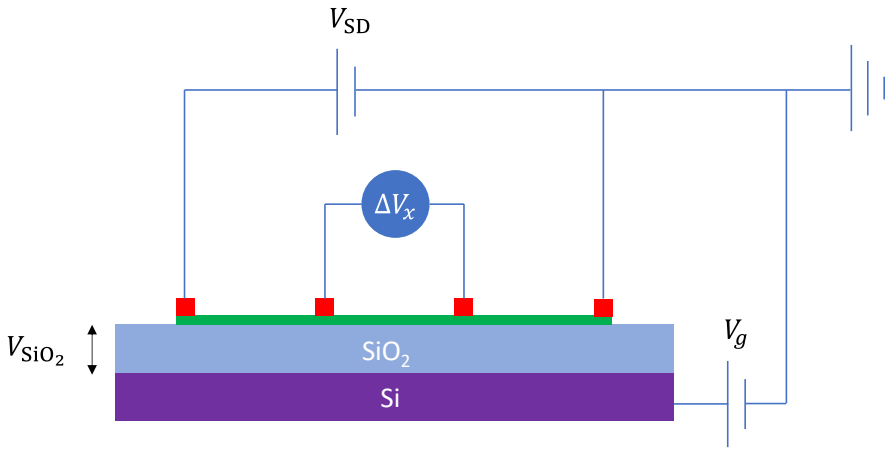

Fig. S5: schematic overview of the graphene field effect transistor

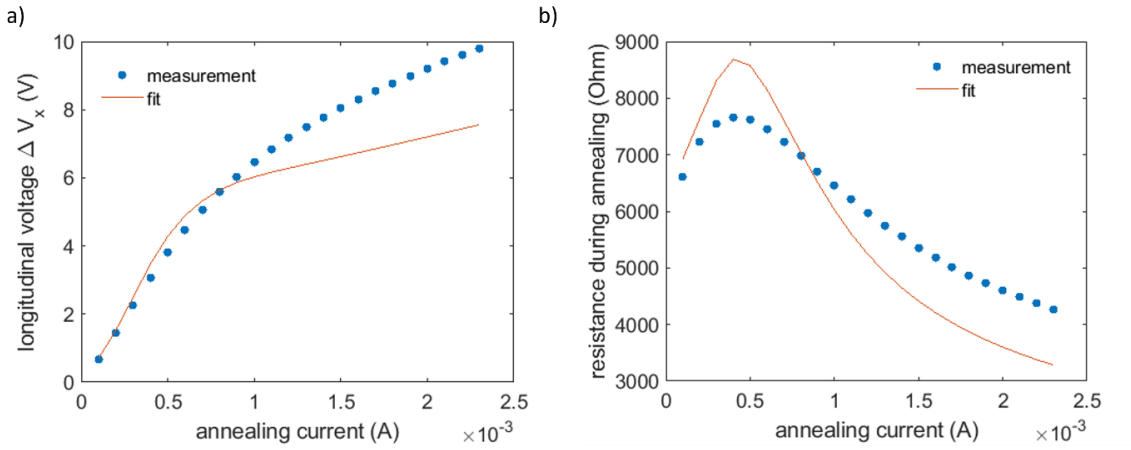

Fig. S6: a) Evolution of ΔV_x during the annealing routine as a function of annealing current. b) Evolution of the resistance of the graphene strip between the voltage contacts.

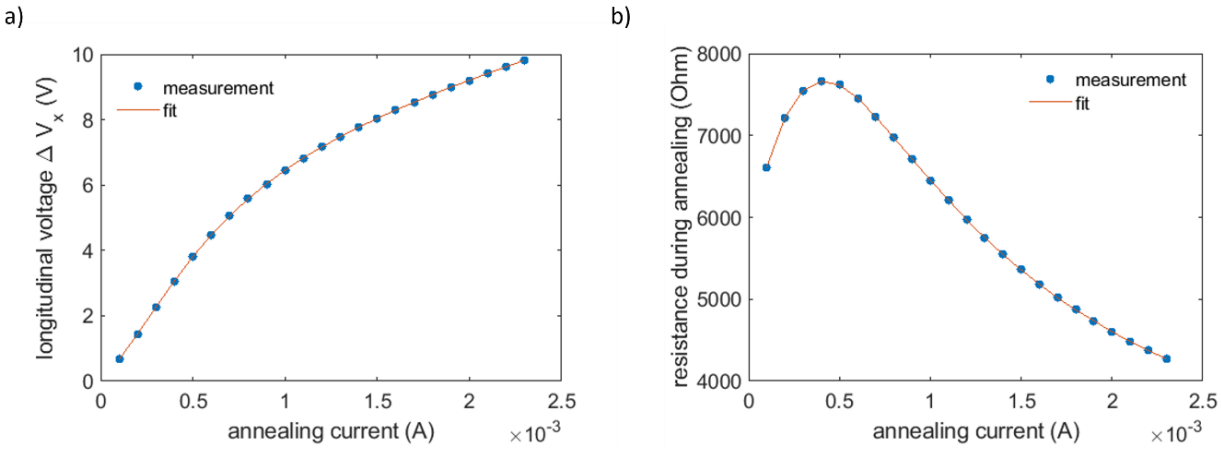

Fig. S7: a) Evolution of ΔV_x during the annealing routine as a function of annealing current. The shift in V_{CNP} is left as a fitting parameter. b) Idem for the evolution of the resistance of the graphene strip between the voltage contacts.

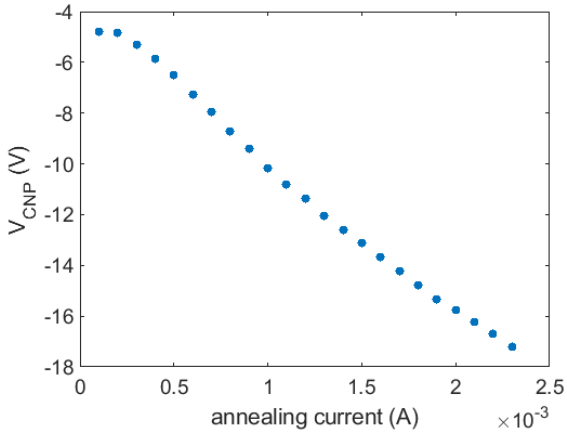

Fig. S8: Evolution of V_{CNP}, as obtained from the fit in Fig. S7.

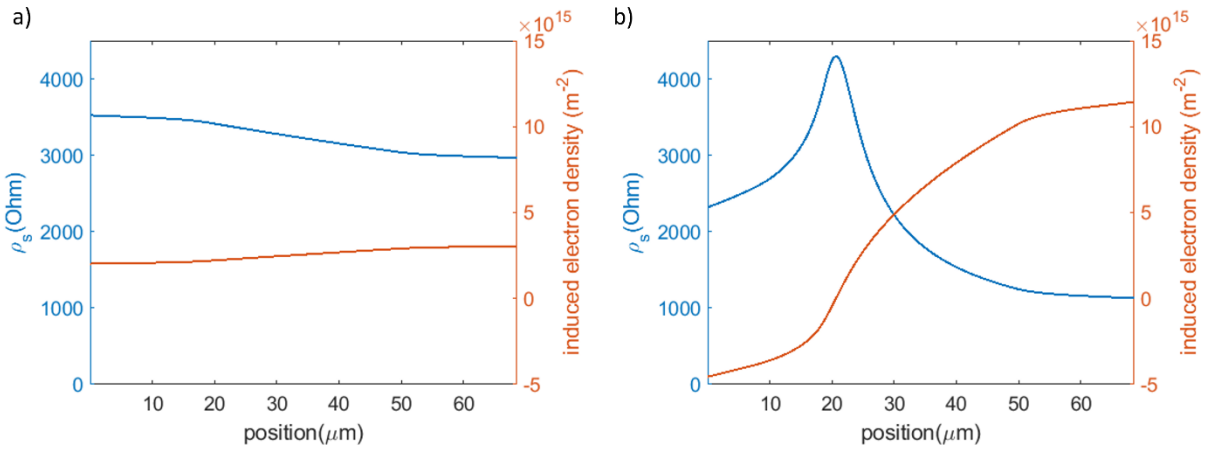

Fig. S9: Sheet resistivity and induced electron density as a function of position in the graphene strip for applied annealing currents of a) 0.1 mA and b) 2.3 mA.

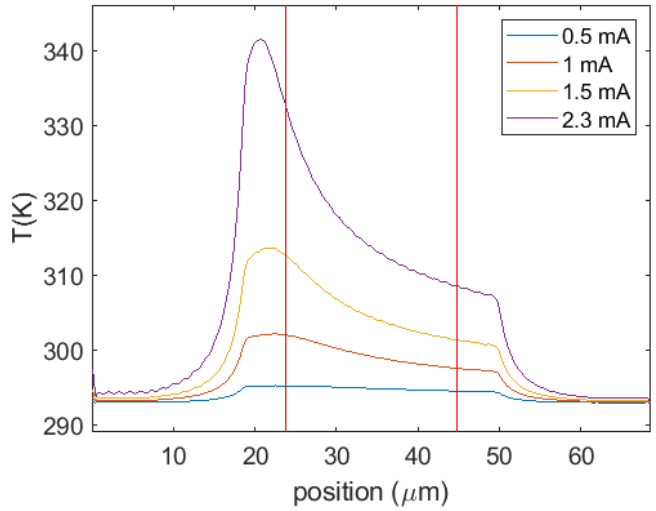

Fig. S10: Temperature profile in the graphene strip for different annealing currents. The red lines indicate the position of the voltage contacts.

6. Correlation analysis $\Delta E^{\ddagger}$ and $\Delta S^{\ddagger}$

When the number of desorbed particles is fitted with formula (9) as defined in the main text, it is important to take into account the correlation between $\Delta E^{\ddagger}$ and $\Delta S^{\ddagger}$. In the following section, the influence of correlation on the error bars of $\Delta E^{\ddagger}$ and $\Delta S^{\ddagger}$ is explained. To estimate the error bars, the χ^2-function can be calculated

$$\chi^2\left(\Delta E^{\ddagger}, \Delta S^{\ddagger}\right) = \frac{\sum_i \left(N_{\mathrm{D,exp},i} - N_{\mathrm{D},i}\right)^2}{\sigma^2}$$

with $N_{\mathrm{D,exp},i}$ the experimentally determined number of desorbed particles after the *i*th current pulse, $N_{\mathrm{D},i}$ the fitted value, and σ the error on the $N_{\mathrm{D,exp},}$ values, which was estimated to be $5 \cdot 10^5$. The χ^2-function is minimal for the optimal values $\Delta E^{\ddagger *}$ and $\Delta S^{\ddagger *}$. It can be shown that $\chi^2\left(\Delta E^{\ddagger *} \pm \sigma_{\Delta E^{\ddagger}}, \Delta S^{\ddagger *}\right) = \chi^2\left(\Delta E^{\ddagger *}, \Delta S^{\ddagger *}\right) + 1$ and analogously for $\Delta S^{\ddagger}$. The plots of χ^2 varied around the two parameters are shown in Fig. S11. Based on these plots alone, one would arrive at error bars of $\sigma_{\Delta E^{\ddagger}} = 0.001$ eV and $\sigma_{\Delta S^{\ddagger}} = 3 \cdot 10^{-6}$ eV/K. However, these error bars do not take into account the effect of correlation between the two fit parameters. In Fig. S12, a plot is shown of the χ^2 function varied for both $\Delta E^{\ddagger}$ and $\Delta S^{\ddagger}$ around the optimal values. The extremal values for $\Delta E^{\ddagger *}$ and $\Delta S^{\ddagger *}$ values where χ^2 is lower than $\chi^2\left(\Delta E^{\ddagger *}, \Delta S^{\ddagger *}\right) + 1$ are with dotted lines. These intervals are equally likely as the values of the intervals indicated in Fig. S11. For this reason, the maximal and minimal values for $\Delta E^{\ddagger}$ and $\Delta S^{\ddagger}$ of the yellow area are taken as the boundaries of the confidence interval for both parameters. These extremal values are also indicated in Fig. S12. In this way, one obtains as error bars $\sigma_{\Delta E^{\ddagger}} = \pm 0.08$ eV and $\sigma_{\Delta S^{\ddagger}} = \pm 0.0003$ eV/K.

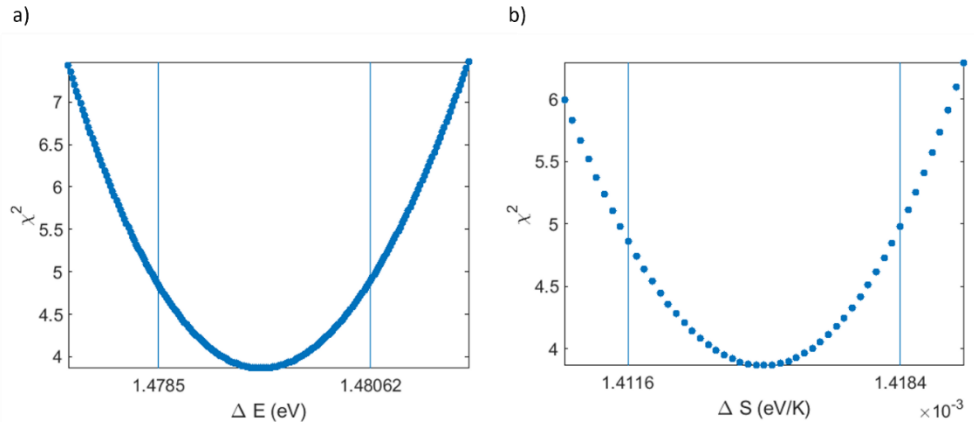

Fig. S11: the χ^2 function varied around the optimal values of the a) energy and b) entropy of the transition state

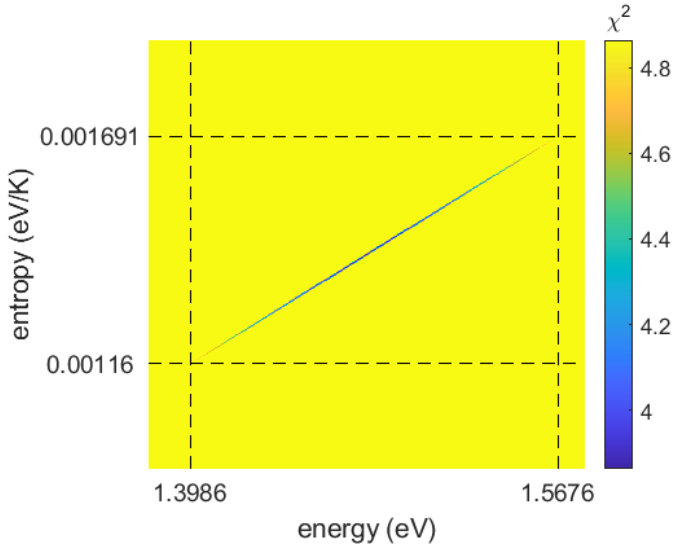

Fig. S12: the χ^2 function varied around the optimal values $\Delta E^{\ddagger *}$ and $\Delta S^{\ddagger *}$. The extremal values for $\Delta E^{\ddagger *}$ and $\Delta S^{\ddagger *}$ where χ^2 is lower than $\chi^2(\Delta E^{\ddagger *},\ \Delta S^{\ddagger *}) + 1$ are indicated with dotted lines.

7. Further details of molecular dynamics simulations and entropy estimation

Table S1: *Statistical analysis of the gold-gold distances in the molecular dynamics simulations*

Without oxygen

Gold atoms	Time average of the distance [Å]	Standard deviation [Å]
atom1-atom2	2.882	0.5272
atom1-atom3	3.575	1.1509
atom2-atom3	3.385	1.0409

With oxygen

Gold atoms	Time average of the distance [Å]	Standard deviation [Å]
atom1-atom2	2.721	0.1839
atom1-atom3	2.980	0.6045
atom2-atom3	3.511	0.9623

Entropy estimation

As described in the main text, the contribution of the vibrations plays the greatest role in the entropy change during oxygen dissociation. Based on the quasi-harmonic-approximation[6,7], the vibrational entropy can be obtained using the following formula[8]:

$$S_{vib} = k_B(3N-n)\int_0^\infty \left\{\frac{\hbar\omega}{2k_BT}\coth\left(\frac{\hbar\omega}{2k_BT}\right) - \ln\left[2\sinh\left(\frac{\hbar\omega}{2k_BT}\right)\right]\right\} D(\omega)d\omega,$$

where k_B is the Boltzmann-constant, $(3N-n)$ are the degrees of freedoms (N is the number of atoms and n is the number of external degrees of freedom, which is 0 in our case), $\hbar$ is the reduced Planck-constant, T is the absolute temperature, $D(\omega)$ is the vibrational density of states (VDOS) and ω is the vibrational frequency. The external temperature is set to 300K, so only the VDOS must be determined. The VDOS can be obtained from the Fourier-transform of the velocity autocorrelation function (VACF) using the Wiener-Khinchin-theorem[9]:

$$D(\omega) = \left|\int_{-\infty}^{\infty} \boldsymbol{v}(t)e^{-i\omega t}dt\right|^2.$$

In this case, $\boldsymbol{v}(t)$ is the velocity of the given nucleus. We obtained the velocities from the MD simulations. While the total simulation time is 10 ps, we used only the trajectory between 1 to 9 ps for the computation. The calculation of the vibrational entropy was based on the equations - mentioned above - and implemented in Python, using a part of the pwtools package developed by Steve Schmerler[10]. Furthermore, the vibrational and total entropy of an isolated oxygen molecule was evaluated using harmonic approximation employing the PBE/def2-TZVP method in the Q-Chem 5.4 program package[11]. The difference in entropies of the bound (graphene + cluster + oxygen) and unbound (graphene + cluster and oxygen) states of the system are computed as follows:

$$\Delta S^{(1)} = {S_{vib}}^{GraAu3} + {S_{tot}}^{O2} - {S_{vib}}^{GraAu3O2},$$

where ${S_{vib}}^{GraAu3}$ and ${S_{vib}}^{GraAu3O2}$ are the vibrational entropies coming from the MD simulations, ${S_{tot}}^{O2}$ is the total entropy calculated using the harmonic approximation. The entropy change between the bound and physisorbed state was also examined, where only the vibrational entropy of the oxygen molecule ${S_{vib}}^{O2}$ was considered:

$$\Delta S^{(2)} = {S_{vib}}^{GraAu3} + {S_{vib}}^{O2} - {S_{vib}}^{GraAu3O2}.$$

Table S2. Estimated entropy values

	System	Vibrational entropy [meV/K]	Total entropy [meV/K]
molecular dynamics	graphene+Au_3+O_2	66.62	
molecular dynamics	graphene+Au_3	68.902	
harmonic approximation	O_2	0.00039	2.031

	Entropy change [meV/K]
bound-unbound states	4.307
bound-'physisorbed' states	2.276

8. References

1 K. Verguts, Y. Defossez, A. Leonhardt, J. De Messemaeker, K. Schouteden, C. Van Haesendonck, et al., *ECS J. Solid State Sci. and Technol.,* 2018, **7**, M195.

2 L. M. Yang, M. Dornfeld, T. Frauenheim and E. Ganz, *Phys. Chem. Chem. Phys.,* 2015, **17**, 26036-26042.

3 M. K. Srivastava, Y. Wang, A. F. Kemper and H. P. Cheng, *Phys. Rev. B,* 2012, **85**, 165444.

4 J. Yan and M. S. Fuhrer, *Phys. Rev. Lett.,* 2011, **107**, 206601.

5 M. H. Bae, Z. Y. Ong, D. Estrada and E. Pop, *Nano Lett.,* 2010, **10**, 4787-4793.

6 K. Alexopoulos, M. S. Lee, Y. Liu, Y. Zhi, Y. Liu, M. F. Reyniers, et al., *J. Phys. Chem. C,* 2016, **120**, 7172-7182.

7 R. L. De Sousa and H. W. Alves, *Braz. J. Phys.,* 2006, **36**, 501-504.

8 G. Collinge, S. F. Yuk, M. T. Nguyen, M. S. Lee, V. A. Glezakou and R. Rousseau, *ACS Catal.,* 2020 **10**, 9236-9260.

9 N. Wiener, *Acta Math.,* 1930, **55**, 117-258.

10 S. Schmerler, "elcorto/pwtools Python package," https://zenodo.org/record/5640089#.YklHguhByUk.

11 E. Epifanovsky, A. T. Gilbert, X. Feng, J. Lee, Y. Mao, N. Mardirossian, et al., *J. Chem. Phys.,* 2021, **155**, 084801.